Role of self-torques in transition metal dichalcogenide/ferromagnet bilayers

Jan Hidding [1,*] Klaiv Mërtiri,[1] Fauzia Mujid,[2] Ce Liang,[2] Jiwoong Park,[2] and Marcos H. D. Guimarães [1,†]

[1]*Zernike Institute for Advanced Materials, University of Groningen, 9747 AG Groningen, The Netherlands*
[2]*Department of Chemistry, Pritzker School of Molecular Engineering, and James Franck Institute,*
University of Chicago, Chicago, Illinois 60637, USA

In recent years, transition metal dichalcogenides (TMDs) have been extensively studied for their efficient spin-orbit torque generation in TMD/ferromagnetic bilayers, owing to their large spin-orbit coupling, large variety of crystal symmetries, and pristine interfaces. Although the TMD layer was considered essential for the generation of the observed spin-orbit torques (SOTs), recent reports show the presence of a self-torque in single-layer ferromagnetic devices with magnitudes comparable to TMD/ferromagnetic devices. Here, we perform second-harmonic Hall SOT measurements on metal-organic chemical vapor deposition (MOCVD) grown MoS_2/permalloy/Al_2O_3 devices and compare them to a single-layer permalloy/Al_2O_3 device to accurately disentangle the role of self-torques, arising from the ferromagnetic layer, from contributions from the TMD layer in these bilayers. We report a fieldlike spin-torque conductivity of $\sigma_{FL} = (-2.8 \pm 0.3) \times 10^3 \frac{\hbar}{2e}(\Omega\,\mathrm{m})^{-1}$ in a single-layer permalloy/Al_2O_3 device, which is comparable to our MoS_2/permalloy/Al_2O_3 devices and previous reports on similar TMD/ferromagnetic bilayers, indicating only a minor role of the MoS_2 layer. In addition, we observe a comparatively weak dampinglike torque in our devices, with a strong device-to-device variation. Finally, we find a linear dependence of the SOT conductivity on the Hall bar arm/channel width ratio of our devices, indicating that the Hall bar dimensions are of significant importance for the reported SOT strength. Our results accentuate the importance of delicate details, like device asymmetry, Hall bar dimensions, and self-torque generation, for the correct disentanglement of the microscopic origins underlying the SOTs, essential for future energy-efficient spintronic applications.

I. INTRODUCTION

Manipulating the magnetization of a magnetic layer by means of a charge current holds an immense promise for more energy-efficient ways of storing and writing information [1–3]. By first converting a charge current into a spin current in materials with large spin-orbit coupling (SOC), the spin current can subsequently exert a torque on the magnetization of an interfaced magnetic material [3]. These current-induced torques, originating from the spin-orbit interaction, are referred to as spin-orbit torques (SOTs). To maximize the SOT strength, an efficient charge-to-spin conversion is advantageous and, thus, materials with large spin-orbit coupling (Pt [4–6], Pd [7–9], W [10,11], Ta [12–14], Hf [15–17], etc.) have been extensively studied [18]. Two main mechanisms for the charge-to-spin conversion in these materials are the spin-Hall effect (SHE) and the Rashba-Edelstein effect (REE) [3,19]. For polycrystalline spin-Hall metals with inversion symmetry, these effects, however, do not possess the ideal symmetry for field-free switching of the magnetization of magnetic layers with perpendicular magnetic anisotropy (PMA) used in modern high-density memory storage [20,21]. While epitaxially grown heavy metals have shown an increase in their SOTs compared to their

polycrystalline counterparts [22,23], as long as their inversion symmetry remains intact, no deterministic field-free switching is expected. Multiple methods have been employed to break the inversion symmetry, such as wedged shaped geometries, vertical composition gradients, or interlayer exchange coupling to an additional in-plane exchange-biased magnetic layer, to allow for field-free switching using standard spin-Hall metals [21,24,25]. However, the search for the out-of-plane dampinglike torque, ideal for switching PMA magnets, lead to the investigation of other, more exotic materials, such as topological insulators and two-dimensional (2D) van der Waals crystals, to search for new materials which allow for energy efficient field-free switching [19,26–29].

In this regard, the family of 2D van der Waals materials called the transition metal dichalcogenides (TMDs) have gained much interest as spin source material, owing to their large SOC, atomically flat surfaces, and broad range of crystal symmetries [20,30,31]. The more conventional and well known semiconducting TMDs, such as WSe_2 [32–34], WS_2 [35], and MoS_2 [34,36], were studied first, due to their air stability, and developed wafer-scale growth. More recently, however, the low symmetry TMDs have gained much interest since the observation of the out-of-plane dampinglike torque in TMD/FM bilayers, which is optimal for switching magnets with PMA [37–43].

Previous reports on SOTs in TMD/ferromagnetic (FM) bilayers often consider the TMD as essential for the generation of the observed SOTs, either through bulk effects, such

*jan.hidding@rug.nl
†m.h.guimaraes@rug.nl

as the spin-Hall effect, or effects arising from the TMD/Py interface, such as the Rashba-Edelstein effect, spin-orbit filtering, or spin-orbit precession [44,45]. More recent reports, however, indicate the presence of a self-torque in single-layer ferromagnetic devices without the presence of a spin source material. A recent study performed magneto-optic Kerr effect (MOKE) measurements to probe the SOT at the surface of a single-layer Py device and observe a sizable SOT at the Py interface, which is ascribed to a SHE in the Py [46]. Also, electrical measurements on Py capped with SiO_2 or Al_2O_3 show the presence of fieldlike and dampinglike torques in Py devices [47]. And, in metallic bilayers, it was shown that self-induced torques lead to errors in the estimation of the spin-torque strength [48]. These self-torques in ferromagnetic materials make it difficult to accurately determine to what extent the TMD layer is contributing to the SOT [47].

Here, we report second-harmonic Hall measurements on MoS_2/Py/Al_2O_3 and single-layer Py/Al_2O_3 devices to disentangle the contribution of self-torques from the FM layer and more accurately determine the effect of the MoS_2 layer. First, we show that the fieldlike self-torque in a single-layer Py/Al_2O_3 device can be of similar magnitude compared to MoS_2/Py/Al_2O_3 devices, indicating a minor effect of the TMD. Second, we find strong device-to-device variations on the dampinglike torque, showing that interface and device quality can strongly affect our signals and potentially indicating that spurious effects can mimic the behavior of the dampinglike torque in these devices. In addition, we study the dependence of the measured spin-orbit torque on the contact/channel width ratio and find a linear dependence of the fieldlike spin-torque conductivity on the Hall arm/channel width ratio. These results indicate the importance of single-layer reference samples and the device geometry for an accurate determination of the microscopic mechanisms underlying the spin-orbit torques.

II. RESULTS AND DISCUSSION

To compare the SOTs in TMD/Py devices with the self-torques in single-layer Py devices, we fabricate both MoS_2/Py/Al_2O_3 and Py/Al_2O_3 Hall bar devices. Below, we discuss the results from both devices separately. Lastly, we discuss the effect of the Hall bar geometry on the measured SOT using harmonic Hall measurements.

A. MoS_2/Py/Al_2O_3 devices

We use wafer-scale grown MoS_2 obtained by metal-organic chemical vapor deposition (MOCVD) [49]. The MOCVD grown MoS_2 layer is characterized using photoluminescence (PL) microscopy and Raman spectroscopy [see Fig. 1(b)] before device fabrication. The two characteristic bands of monolayer MoS_2 at 385 cm^{-1} and 405 cm^{-1}, corresponding to the in-plane (E_{2g}^1) and out-of-plane phonon mode (A_{1g}), respectively, are clearly observed, as indicated in Fig. 1(b) [50]. Furthermore, a strong and homogeneous PL is obtained using PL microscopy shown in the insets of Fig. 1(b), indicating the homogeneous coverage of monolayer MoS_2 with little strain on the substrate.

Next, multiple MoS_2/Py/Al_2O_3 Hall bar devices were fabricated to perform the harmonic Hall measurements. An ac current (I_0) ranging from 500 to 700 μA is applied and the first (V_{xy}^ω) and second ($V_{xy}^{2\omega}$) harmonic Hall voltage are measured while an applied magnetic field (H) is rotated in-plane, making an angle ϕ with respect to the current direction [Fig. 1(c); the details are described in the Methods section]. When assuming a small in-plane magnetic anisotropy compared to $\mu_0 H$, the magnetization is aligned with the external magnetic field and the first-harmonic Hall voltage (V_{xy}^ω) is given by [5,51,52]

$$V_{xy}^\omega(\phi) = I_0 R_{PHE} \sin(2\phi) + I_0 R_{AHE} \cos(\theta), \quad (1)$$

where θ is the magnetic field's polar angle ($\theta = 90°$ for in-plane measurements) and the R_{PHE} and R_{AHE} are the planar Hall and anomalous Hall effect resistance. The first-harmonic Hall voltage (V_{xy}^ω), depicted in Fig. 1(d) for a magnetic field of 40 mT, follows a clear $\sin(2\phi)$ behavior due to the planar Hall effect of the Py layer. By fitting the data to Eq. (1) we obtain a planar Hall resistance of $R_{PHE} = 0.40 \pm 0.03$ Ω. In previous reports on exfoliated TMD/FM bilayers, large deviations from the $\sin(2\phi)$ dependence were observed at low magnetic fields, indicating that a strong uniaxial magnetic anisotropy was induced in the Py [32,39,42,43]. In these reports, the induced anisotropy was attributed to a strong interaction between the Py and the crystalline structure of the underlying TMD. As the MOCVD grown TMD in our devices has a grain size of around 1 μm, our Hall bar covers multiple domains [49]. Therefore, no induced magnetic anisotropy in the Py from the TMD crystal structure is expected. This is in line with our observation, as only minor deviations from the $\sin(2\phi)$ fit are observed. For devices with a smaller Hall bar arm width/channel width ratio, these minor deviations disappear completely, indicating that the minor deviations observed for narrow Hall bars are likely due to shape anisotropy of the Hall bar.

To determine the fieldlike (τ_{FL}) and dampinglike torques (τ_{DL}), the second-harmonic Hall (SHH) voltage is measured [Fig. 1(e)]. The SHH voltage can be described by [5,51]

$$V_{xy}^{2\omega}(\phi) = A \cos(2\phi)\cos(\phi) + B \cos(\phi), \quad (2)$$

where the A and B components are given by

$$A = \frac{R_{PHE} I_0 \tau_\perp / \gamma}{H}, \quad (3)$$

$$B = \frac{R_{AHE} I_0 \tau_\parallel / \gamma}{H + H_K} + I_0 R_{ANE}. \quad (4)$$

Here, γ is the gyromagnetic ratio, H_K is the out-of-plane anisotropy field, and R_{ANE} is the anomalous Nernst resistance. Since our signals are consistent with only the presence of out-of-plane fieldlike torques and in-plane antidamping torques, we will assume here that $\tau_\perp \equiv \tau_{FL} \propto (\hat{m} \times \hat{y})$ and $\tau_\parallel \equiv \tau_{DL} \propto \hat{m} \times (\hat{y} \times \hat{m})$. The SHH is fitted using Eq. (2) to extract the amplitude of the A and B components. As can be seen from Fig. 1(e), our data is well described by Eq. (2). Subsequently, the A and B components are determined for different magnetic fields, allowing us to obtain the τ_{FL}, τ_{DL}, and anomalous Nernst resistance (R_{ANE}) using Eq. (3) and Eq. (4). For the MoS_2/Py/Al_2O_3 devices, we corrected our data for a systematic 15 mT offset in the field due to a
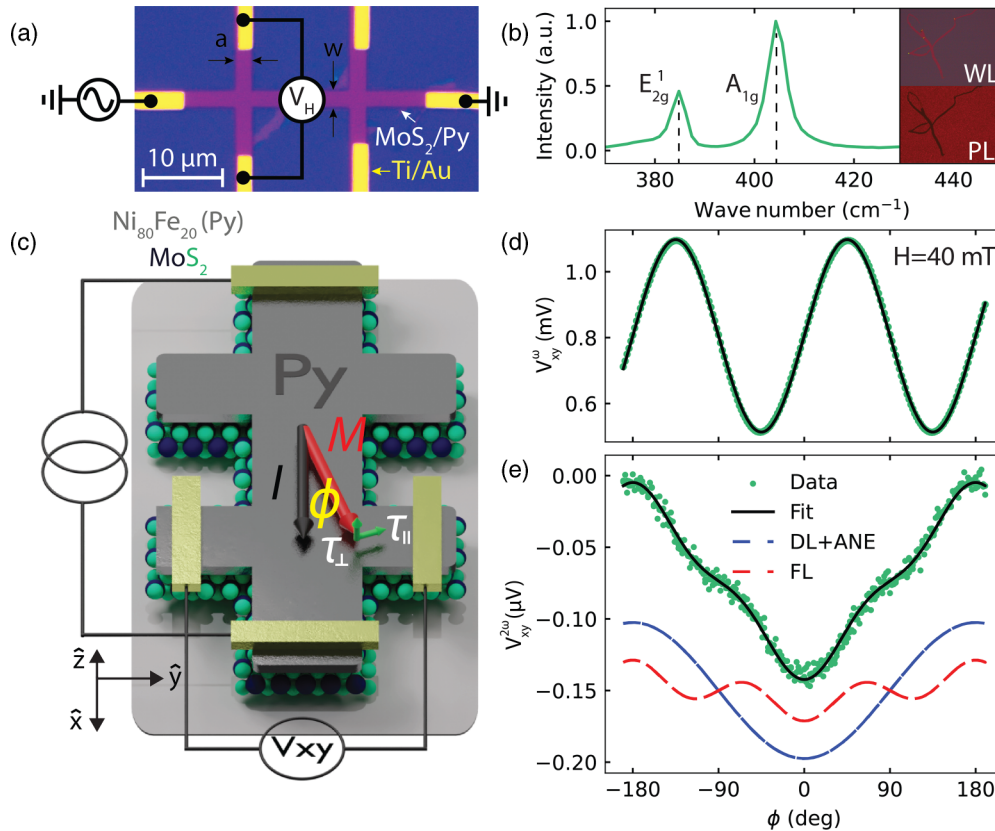
FIG. 1. (a) Optical micrograph of an actual MOCVD MoS_2/Py/Al_2O_3 device. (b) A Raman spectrum of the MOCVD grown MoS_2 showing the characteristic E_{2g}^1 and A_{1g} modes of MoS_2. The two insets on the right depict a white light (WL) and photoluminescence (PL) micrograph of a scratch in the MOCVD grown MoS_2 layer, indicating a strong PL from the monolayer MoS_2. (c) A schematic of a SOT device with the measurement geometry schematically depicted. A low frequency ac current I (black arrow) is applied through the channel and the first- and second-harmonic Hall voltage ($V_{xy}^{\omega(2\omega)}$) are simultaneously measured while the magnetization of the permalloy M (red arrow) is rotated in-plane by an external magnetic field. The current induced in-plane (dampinglike) and out-of-plane (fieldlike) SOTs are depicted with the green arrows $\tau_\parallel$ and $\tau_\perp$, respectively. (d) The measured first-harmonic and (e) second-harmonic Hall voltage versus in-plane angle of the applied magnetic field (40 mT). (d) A clear $\cos(2\phi)$ dependence is observed due to the planar Hall effect of the Py. (e) The second-harmonic Hall voltage (blue points) is fitted (black line) using Eq. (2). The dashed blue and red lines indicate the separate $\cos(\phi)\cos(2\phi)$ and $\cos(\phi)$ components from Eq. (2), related to the fieldlike and dampinglike torque, respectively.

residual current in our electromagnet. The $R_{AHE} = 0.15\ \Omega$ is obtained by performing a separate measurement where the first harmonic Hall voltage is measured while sweeping the magnetic field out-of-plane from approximately -1 T to 1 T (see the Methods section, Fig. 4).

Figure 2 show the field dependence of the (a) A and (c) B component of a MOCVD MoS_2/Py/Al_2O_3 device. As expected from Eq. (3), the A component shows a linear dependence on the inverse magnetic field, which clearly indicates the presence of a fieldlike torque τ_{FL}. For the four separate devices, we find a spread in the fieldlike spin-torque conductivity σ_{FL}, with a minimum of $(-3.5 \pm 0.2) \times 10^3\ \frac{\hbar}{2e}(\Omega\,m)^{-1}$ and a maximum of $(-7.5 \pm 0.6) \times 10^3\ \frac{\hbar}{2e}(\Omega\,m)^{-1}$ for an applied current density of 0.8×10^{10} A/m^2 to 5×10^{10} A/m^2 (see the Methods section for the spin-torque conductivity calculation).

This value is comparable to previous reports on chemical vapor deposition (CVD) grown MoS_2/CoFeB devices from Shao *et al.* [34] and slightly lower compared to other semiconducting TMD/Py devices (e.g., WS_2, WSe_2) [32–35]. Larger fieldlike torques are reported in semimetallic TMD/Py

bilayers, which is explained by the considerable Oersted torque arising from the current flowing through the conducting TMD [37,39,42]. Using four-probe measurements, we find a square resistance R_{sq} for the Py layer of 101.4 Ω. The sheet resistance reported for the MOCVD grown MoS_2 layer, on the other hand, are much higher than the sheet resistance of Py even for heavily doped layers, ranging from 42 kΩ to 83 kΩ in the transistor on-state [49] at room temperature. Due to the semiconducting character of the MoS_2 layer in our devices, no current is expected to flow through the MoS_2 and thus no Oersted torque is expected.

In the presence of a τ_{DL}, a linear dependence of the B component is expected versus the inverse field [see Eq. (4)]. For only one of our four MoS_2/Py/Al_2O_3 devices, we find a linear dependence of the B component at high fields, as depicted in Fig. 2(c). For the three other devices, we find nonsignificant dampinglike spin-torque conductivities (σ_{DL}) with large errors, with a minimum σ_{DL} of $(-4 \pm 32) \times 10^3\ \frac{\hbar}{2e}(\Omega\,m)^{-1}$ and a maximum σ_{DL} of $(3 \pm 3) \times 10^5\ \frac{\hbar}{2e}(\Omega\,m)^{-1}$. Additionally, we observe large deviations from the linear dependence at low
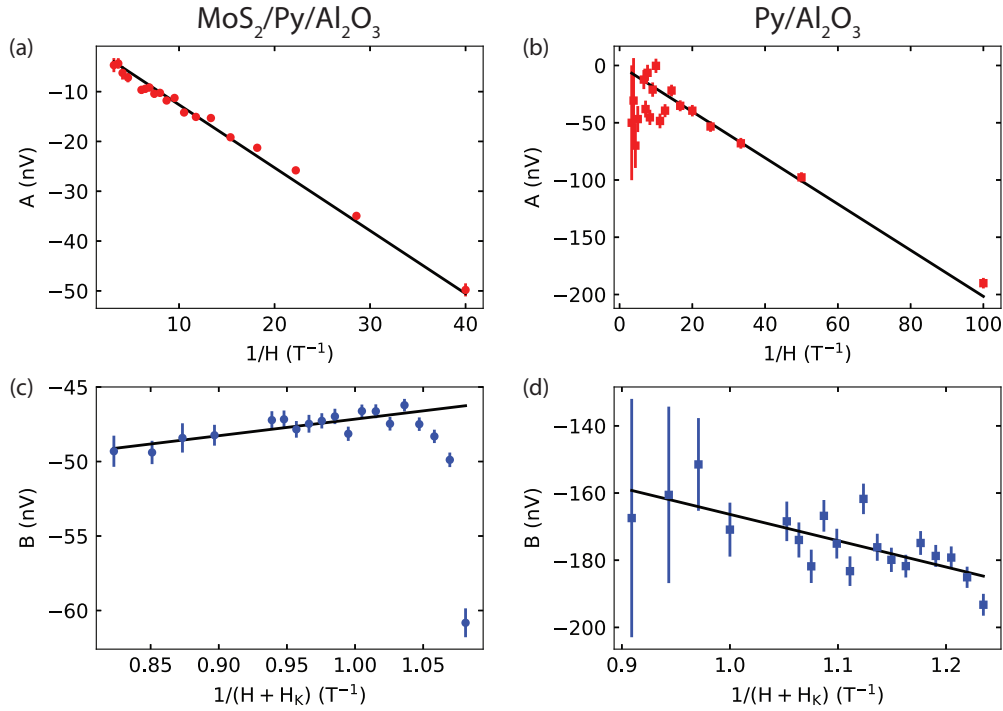
FIG. 2. A and B components from Eq. (2) versus the inverse magnetic field for a $MoS_2/Py/Al_2O_3$, (a) and (c), and single-layer Py/Al_2O_3, (b) and (d), device, respectively. The components were obtained by fitting the second-harmonic Hall voltage [as depicted in Fig. 1(e)] to Eq. (2) for multiple external magnetic field strengths. A clear linear dependence is observed for the A component in both devices and is fitted to Eq. (3) to obtain the fieldlike torque τ_{FL}. Especially for the $MoS_2/Py/Al_2O_3$ device, the B component deviates from the linear trend at low magnetic fields, which could be due to electron-magnon scattering. For the $MoS_2/Py/Al_2O_3$ devices, we therefore neglected the fields at low fields (10 mT, 20 mT, and 30 mT) to obtain a better linear fit. Furthermore, we corrected our data for a systematic offset of 15 mT in the applied field.

fields in Fig. 2(c). This can be explained by the fact that Eq. (3) and Eq. (4) are derived assuming that $H \gg H_A$, where H_A is the in-plane uniaxial anisotropy field, which does not hold anymore at low magnetic fields [51]. To get a more accurate estimate of the dampinglike torque in this device, we therefore neglect the three data points at lowest field when fitting the data to Eq. (4). For this single device, we find a dampinglike spin-torque conductivity σ_{DL} of $(1.2 \pm 0.3) \times 10^5 \frac{\hbar}{2e}(\Omega\,m)^{-1}$. This value is comparable to values reported in SOT devices made with Pt, W, and $NiPS_3$, and is significantly higher compared to SOT devices using other TMDs (e.g., WTe_2, $MoTe_2$, WSe_2, etc.). The presence of both a fieldlike and dampinglike torque in MoS_2/Py has been previously reported by Zhang *et al.* in ST-FMR measurements [36]. There, a torque ratio of $\tau_{FL}/\tau_{DL} = 0.19 \pm 0.01$ is reported, indicating a five times stronger dampinglike torque. Similarly, we find a stronger dampinglike torque for this one device, showing a dampinglike torque a factor of 20 stronger than the fieldlike torque. On the other hand, Shao *et al.* report no dampinglike torque in their SHH measurements on $MoS_2/CoFeB$ bilayers [34], similar to our other devices. These contrasting observations show that there is a significant device-to-device variation for the dampinglike torque in these bilayers. This is highlighted by the fact that we observe no significant dampinglike torques in three of our four devices. Furthermore, it was shown that the ordinary Nernst effect can contribute to spurious second harmonic Hall voltages in these types of measurements, leading to a linear dependence of the B component on the external

magnetic field [53]. The absence of a clear linear dependence of the B component on the external magnetic field strength for all $MoS_2/Py/Al_2O_3$ and single-layer Py/Al_2O_3 devices indicates that this effect does not play a major role in our devices.

B. Single-layer Py/Al_2O_3 device

To determine the contribution of possible self-torques in the Py layer and accurately resolve the effect of the MOCVD grown MoS_2 layer on the SOTs, we compare the SOT measurements from the $MoS_2/Py/Al_2O_3$ device to a single-layer Py/Al_2O_3 reference device. In Figs. 2(b) and 2(d) the A and B components for the single-layer Py/Al_2O_3 device are plotted versus the inverse field. Surprisingly, even without the MoS_2 layer, we observe a clear linear dependence for the A component similar to the $MoS_2/Py/Al_2O_3$ devices, indicating the presence of a fieldlike self-torque. Using Eq. (3) and Eq. (5), we find $\sigma_{FL} = (-2.8 \pm 0.3) \times 10^3 \frac{\hbar}{2e}(\Omega\,m)^{-1}$. The σ_{FL} has the same sign and its magnitude is only 25% lower compared to the $MoS_2/Py/Al_2O_3$ device, which indicates that the presence of the TMD layer does not significantly enhance the fieldlike SOT conductivity.

For the B component, however, no large deviations at low fields are observed, as was the case with the $MoS_2/Py/Al_2O_3$ device. Using Eq. (3) and Eq. (5), we find $\sigma_{DL} = (-2.6 \pm 0.6) \times 10^5 \frac{\hbar}{2e}(\Omega\,m)^{-1}$, which is larger and has an opposite sign compared to the single $MoS_2/Py/Al_2O_3$ device that did show a significant dampinglike torque. For other Py/Al_2O_3

samples, however, no clear dampinglike torques were observed, suggesting that the dampinglike torque is strongly dependent on device (interface) specifics. This indicates that either the origin of the dampinglike self-torque stems from different skew-scattering mechanisms which are dependent on interface and material quality, an inhomogeneous current distribution, or that the field dependence of the B component is due to spurious effects which mimic the behavior of the dampinglike torque, such as unidirectional magnetoresistance due to electron-magnon scattering [54,55]. The opposite sign could result from the different material interfaces of the Py, which could give rise to different scattering events, resulting in a different dampinglike SOT [28,56]. However, as the magnitude of the dampinglike torque is unrealistically high, comparing to the dampinglike torque strength observed in Pt/Py samples, we believe that the field dependence of the B component is due to spurious effects at low magnetic fields or an inhomogeneous current flow in these devices.

Other reports on single-layer Py devices show both a field-like and a dampinglike torque in ST-FMR measurements [47]. Seki *et al.* observe a fieldlike torque in all their single-layer Py devices, but only observe a dampinglike torque in devices where the structural inversion symmetry was broken due to different interfaces of the Py layer. In our devices, the structural inversion symmetry is broken as well, as the Py is evaporated on SiO_2 and capped with Al_2O_3 and thus possesses two different interfaces. A difference in electron-scattering from these two interfaces could, in turn, lead to a self-torque. Furthermore, Seki *et al.* report only dampinglike torques for devices where the Py layer is sufficiently thin ($\leqslant 3$ nm), which could explain why we do not observe a reliable dampinglike torque for our Py devices of 6 nm [47]. Also, Schippers *et al.* report measurements on a similar single-layer Py reference sample with a 6 nm Py thickness, capped with Al_2O_3 [57]. At room temperature, they find a σ_{FL} which is three times larger and a σ_{DL} which is one order of magnitude smaller. For their samples, however, the layers are deposited using magnetron sputtering, while our samples employed electron beam evaporation, which could lead to different material and interface qualities and different current distributions in the Py layer.

All these different torque strengths and directions observed for similar MoS_2/FM bilayers and single-layer Py devices underline the large device-to-device variation, also observed in our devices. Our observations show that the self-torque, originating solely from the FM layer, can have a significant contribution to the observed SOTs in TMD/FM bilayers.

C. Effect of the Hall bar dimensions

Lastly, we study the effect of the Hall bar arm width/channel width ratio (a/w), for the MoS_2/Py/Al_2O_3 devices by keeping the arm width constant at $a = 2$ μm, while varying the channel width (w) from 2 μm to 10 μm. In Fig. 3, the raw (a) fieldlike and (b) dampinglike spin-torque conductivities (gray circles) for all devices are plotted versus (a/w). For comparison, the $\sigma_{FL(DL)}$ from the single-layer Py/Al_2O_3 device is included and depicted by the gray unfilled squares. We observe a clear, almost linear, dependence of σ_{FL} on the channel width. The σ_{FL} for the device with $a/w = 0.2$ is a fac-
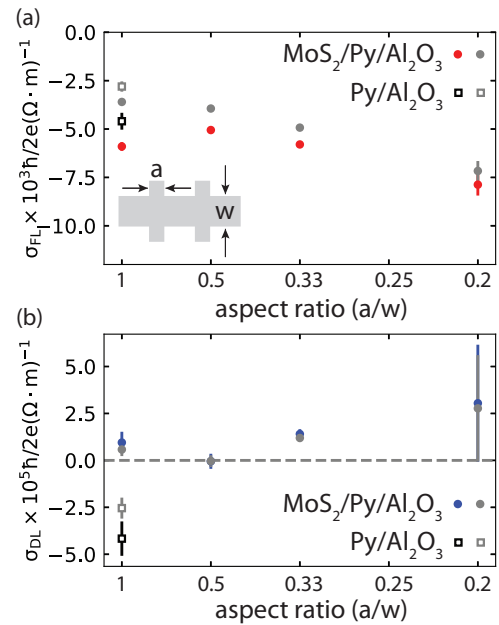

FIG. 3. (a) Fieldlike and (b) dampinglike spin-torque conductivity for the MoS_2/Py/Al_2O_3 devices (circles) and the single-layer Py/Al_2O_3 device (squares) versus the arm width/channel width ratio of the Hall bar. The gray points correspond to the raw spin-torque conductivity and the colored points to the corrected spin-torque conductivity, according to Ref. [58]. The inset in (a) shows the voltage arm width (a) and the channel width (w). For these devices, the arm width is kept constant ($a = 2$ μm), while the channel width is varied.

tor 2 larger than the device with $a/w = 1$. We stress that the larger error bar for the device with $a/w = 0.2$ is ascribed to a smaller current density compared to the other devices. This observation is in line with recent work from Neumann *et al.*, where the arm width/channel width ratio is shown to affect the estimation of the spin-Hall angle (θ_{SH}) [58]. A significantly decreasing θ_{SH} is found when the arm width/channel width ratio becomes sufficiently big ($\geqslant 1$), reporting a value of only 70% at an arm width/channel width ratio of 1. To correct our $\sigma_{FL(DL)}$, we incorporate a factor for each arm width/channel width ratio as reported by Neumann *et al.* [58] and plot the corrected values in Fig. 3 as red (fieldlike) and blue (damping-like) circles (correction factors can be found in the Methods section).

After the correction, there is no clear monotonic decrease of σ_{FL} with the arm width/channel width ratio. However, still some device-to-device variation is found, which could be due to varying interface and material qualities. For σ_{DL}, the reported values for both the MoS_2/Py/Al_2O_3 and the single-layer Py/Al_2O_3 devices remain large with correspondingly large error bars as previously discussed. These results emphasize, and function as experimental evidence for, the importance of the geometrical factors of the Hall bar on the obtained SOT values from harmonic Hall measurements in TMD/Py bilayers. Performing similar measurements of the self-torque dependence on the Hall bar dimensions of the single-layer Py/Al_2O_3 device could shed light on the reliability of the measured self-torques. Therefore, we suggest these measurements be performed on single-layer Py/Al_2O_3

devices with varying arm width/channel width ratios to better characterize the self-torque in FM layers.

III. CONCLUSION

In conclusion, our results indicate that the self-torques, originating from the FM layer, can have significant contributions to the observed SOTs in TMD/FM bilayers. We observe a similar τ_{FL} in single-layer Py/Al$_2$O$_3$ devices, indicating that the MOCVD MoS$_2$ layer in our MoS$_2$/Py/Al$_2$O$_3$ is of minor importance for the generation of fieldlike SOTs. This suggests that the FM layer, rather than the TMD, might play a dominant role in the generation of the observed SOTs in TMD/FM bilayers. Previous contrasting SOT observations in similar TMD/FM bilayers could thus be ascribed to differences in the FM layer (e.g., different fabrication techniques, capping layers, interface quality, etc.) rather than different interactions between the TMD and the FM. We therefore recommend that the self-torque in single-layer FM reference samples is also characterized in future studies in order to accurately determine the effect of the TMD layer on the observed SOTs and that the Hall bar dimensions should be clearly reported. In addition, in HM/FM bilayers, the self-torque in the FM layers could counteract the torque generated by the HM layer, resulting in a reduced net torque. Taking advantage of the self-torques in the FM layer, making them work in conjunction with other SOTs instead, could lead to an increase in the SOT efficiency [48]. Tailoring the FM interfaces to change the self-torque direction and strength, in conjunction with searching for different materials as SOT sources, could be a promising route towards an increase in SOT efficiency. These results pave the way for a more accurate disentanglement of all microscopic mechanisms at play, increasing our understanding of the origins underlying the SOTs, which is essential for more energy efficient magnetic memory devices.

IV. METHODS

A. Device fabrication

The MoS$_2$ layer was grown using metal-organic chemical vapor deposition (MOCVD) on a SiO$_2$(285 nm)/Si substrate as described in Ref. [49]. The MoS$_2$ is characterized with a PL microscope using a BrightLine long-pass filter set to check the homogeneity of the monolayer coverage on the SiO$_2$/Si substrate (see Fig. 1).

Next, a separately prepared PMMA mask with exposed Hall bars of different widths is deposited on top of the MoS$_2$ covered substrate, which ensures a pristine interface between the permalloy and MoS$_2$ with no polymer contamination. Using electron beam evaporation, 6 nm of permalloy and a capping layer and hard mask of 17 nm of Al$_2$O$_3$ are deposited. Subsequently, the contacts are defined using standard e-beam lithography techniques. Then, first an Al$_2$O$_3$ wet etch with tetramethylammonium is performed for 45 s at 40 °C, after which *in situ* Ar milling is performed prior to the evaporation of the Ti/Au (5/55 nm) contacts. Finally, the remaining MoS$_2$ layer is removed using reactive ion etching [CF$_4$ (9.5 sccm)/O$_2$ (0.5 sccm), 30 W RF, 5W ICP, 30 s].
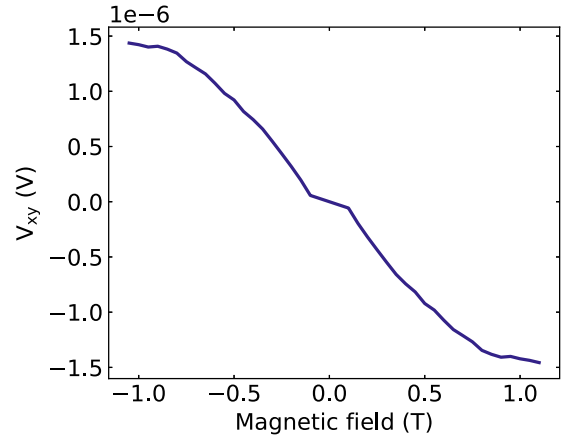

FIG. 4. Antisymmetrized Hall voltage for the anomalous Hall measurement used to obtain the anomalous Hall resistance, R_{AHE}, and the saturation magnetization, M_s, needed to determine τ_{DL} from Eq. (4). The data presented here are antisymmetrized to reduce any errors due to sample misalignment.

B. Electrical measurements

The harmonic Hall measurements, illustrated in Fig. 1(a) and Fig. 1(c), were performed at room temperature using a standard lock-in technique with low frequency (77.77 Hz) ac currents (I_0), ranging from 500 μA to 700 μA [5,51,52]. Subsequently, the first (V_{xy}^{ω}) and second ($V_{xy}^{2\omega}$) harmonic Hall voltage were measured while an applied magnetic field (H), ranging from 10 mT to 300 mT, was rotated in-plane, making an angle ϕ with respect to the current [Fig. 1(c)]. Albeit the different thermal conductivity of MoS$_2$ [59] and SiO$_2$ [12], we find a similar anomalous Nernst voltage for the device width a similar width (2 μm) of -0.13 ± 0.01 mV and -0.13 ± 0.03 mV, respectively.

To better compare the SOTs in our devices to previous reports on SOTs in TMD/FM bilayers, we express the SOT in terms of spin-torque conductivity—the common figure of merit in literature due to its independence on geometric factors [6,42]. The spin-torque conductivity is defined as the total angular momentum absorbed by the ferromagnet per second, per unit interface area, per applied electric field, in units of $\frac{\hbar}{2e}$, and is calculated according to

$$\sigma_{FL(DL)} = \frac{2e}{\hbar} M_s t_{py}(lw) \frac{\tau_{FL(DL)}/\gamma}{(lw)E} = \frac{2e}{\hbar} M_s t_{Py} w \frac{\tau_{FL(DL)}/\gamma}{R_{sq} I_0},$$

(5)

where M_s is the saturation magnetization, $\hbar$ is the reduced Planck's constant, e is the electron charge, E is the electric field, R_{sq} is the square resistance, I_0 is the applied current, and l, w, and t_{Py} are the length, width, and Py thickness, respectively.

To correct the magnitude of $\sigma_{FL/DL}$ according to the arm width/channel width ratio of the different devices, we divided the raw values by the correction factors supplied by Neumann

et al. [58]. These correspond to 0.91, 0.85, 0.78, 0.61, and 0.61 for arm width/channel width ratio of 0.2, 0.33, 0.5, 1, and 1, respectively.

C. Anomalous Hall measurement

To determine the anomalous Hall resistance, R_{AHE}, and the saturation magnetization, M_s, needed for determining the dampinglike torque τ_{DL} using Eq. (4), we performed anomalous Hall measurements (Fig. 4). Using a standard lock-in technique with a low frequency (17.77 Hz) current of 10 μA, the Hall voltage is measured while an out-of-plane magnetic field is swept from ~ -1 T to 1 T, as shown in Fig. 4. To reduce errors from any misalignment, the Hall voltage is antisymmetrized. Assuming that the anisotropy of the Py is solely due to shape anisotropy, the anomalous Hall resistance will saturate when the magnetization is completely saturated in the out-of-plane direction. From the anomalous Hall measurements, we are therefore able to determine that the H_K for our MoS_2/Py/Al_2O_3 devices is 0.9 T, and 0.8 T for the single-layer Py/Al_2O_3, which is taken to be approximately $\mu_0 M_s$ for strong shape anisotropy. This is in agreement with previously reported values for similar thin Py layers [34,42,57].

[1] B. Dieny, I. L. Prejbeanu, K. Garello, P. Gambardella, P. Freitas, R. Lehndorff, W. Raberg, U. Ebels, S. O. Demokritov, J. Akerman, A. Deac, P. Pirro, C. Adelmann, A. Anane, A. V. Chumak, A. Hirohata, S. Mangin, S. O. Valenzuela, M. C. Onbal, M. D'Aquino *et al.*, Nat. Electron. **3**, 446 (2020).

[2] A. Manchon, H. C. Koo, J. Nitta, S. M. Frolov, and R. A. Duine, Nat. Mater. **14**, 871 (2015).

[3] A. Manchon, J. Železný, I. M. Miron, T. Jungwirth, J. Sinova, A. Thiaville, K. Garello, and P. Gambardella, Rev. Mod. Phys. **91**, 035004 (2019).

[4] X. Fan, H. Celik, J. Wu, C. Ni, K.-J. Lee, V. O. Lorenz, and J. Q. Xiao, Nat. Commun. **5**, 3042 (2014).

[5] K. Garello, I. M. Miron, C. O. Avci, F. Freimuth, Y. Mokrousov, S. Blügel, S. Auffret, O. Boulle, G. Gaudin, and P. Gambardella, Nat. Nanotechnol. **8**, 587 (2013).

[6] M.-h. Nguyen, D. C. Ralph, and R. A. Buhrman, Phys. Rev. Lett. **116**, 126601 (2016).

[7] A. Ghosh, K. Garello, C. O. Avci, M. Gabureac, and P. Gambardella, Phys. Rev. Appl. **7**, 014004 (2017).

[8] M. Jamali, K. Narayanapillai, X. Qiu, L. M. Loong, A. Manchon, and H. Yang, Phys. Rev. Lett. **111**, 246602 (2013).

[9] H.-R. Lee, K. Lee, J. Cho, Y.-H. Choi, C.-Y. You, M.-H. Jung, F. Bonell, Y. Shiota, S. Miwa, and Y. Suzuki, Sci. Rep. **4**, 6548 (2014).

[10] K.-u. Demasius, T. Phung, W. Zhang, B. P. Hughes, S.-H. Yang, A. Kellock, W. Han, A. Pushp, and S. S. P. Parkin, Nat. Commun. **7**, 10644 (2016).

[11] C.-F. Pai, L. Liu, Y. Li, H. W. Tseng, D. C. Ralph, and R. A. Buhrman, Appl. Phys. Lett. **101**, 122404 (2012).

[12] C. O. Avci, K. Garello, M. Gabureac, A. Ghosh, A. Fuhrer, S. F. Alvarado, and P. Gambardella, Phys. Rev. B **90**, 224427 (2014).

[13] J. Kim, J. Sinha, M. Hayashi, M. Yamanouchi, S. Fukami, T. Suzuki, S. Mitani, and H. Ohno, Nat. Mater. **12**, 240 (2013).

[14] L. Liu, C.-F. Pai, Y. Li, H. W. Tseng, D. C. Ralph, and R. A. Buhrman, Science **336**, 555 (2012).

[15] M. Akyol, W. Jiang, G. Yu, Y. Fan, M. Gunes, A. Ekicibil, P. Khalili Amiri, and K. L. Wang, Appl. Phys. Lett. **109**, 022403 (2016).

[16] R. Ramaswamy, X. Qiu, T. Dutta, S. D. Pollard, and H. Yang, Appl. Phys. Lett. **108**, 202406 (2016).

[17] J. Torrejon, J. Kim, J. Sinha, S. Mitani, M. Hayashi, M. Yamanouchi, and H. Ohno, Nat. Commun. **5**, 4655 (2014).

[18] T. Tanaka, H. Kontani, M. Naito, T. Naito, D. S. Hirashima, K. Yamada, and J. Inoue, Phys. Rev. B **77**, 165117 (2008).

[19] Q. Shao, P. Li, L. Liu, H. Yang, S. Fukami, A. Razavi, H. Wu, K. Wang, F. Freimuth, Y. Mokrousov, M. D. Stiles, S. Emori, A. Hoffmann, J. Akerman, K. Roy, J.-P. Wang, S.-H. Yang, K. Garello, and W. Zhang, IEEE Trans. Magn. **57**, 1 (2021).

[20] Y. Liu and Q. Shao, ACS Nano **14**, 9389 (2020).

[21] G. Yu, P. Upadhyaya, Y. Fan, J. G. Alzate, W. Jiang, K. L. Wong, S. Takei, S. A. Bender, L.-T. Chang, Y. Jiang, M. Lang, J. Tang, Y. Wang, Y. Tserkovnyak, P. K. Amiri, and K. L. Wang, Nat. Nanotechnol. **9**, 548 (2014).

[22] A. Kumar, N. Behera, R. Gupta, S. Husain, H. Stopfel, V. Kapaklis, R. Brucas, and P. Svedlindh, J. Phys. D **53**, 355003 (2020).

[23] P. Li, L. J. Riddiford, C. Bi, J. J. Wisser, X.-Q. Sun, A. Vailionis, M. J. Veit, A. Altman, X. Li, M. DC, S. X. Wang, Y. Suzuki, and S. Emori, Phys. Rev. Mater. **5**, 064404 (2021).

[24] Y.-C. Lau, D. Betto, K. Rode, J. M. D. Coey, and P. Stamenov, Nat. Nanotechnol. **11**, 758 (2016).

[25] Z. Zheng, Y. Zhang, V. Lopez-Dominguez, L. Sánchez-Tejerina, J. Shi, X. Feng, L. Chen, Z. Wang, Z. Zhang, K. Zhang, B. Hong, Y. Xu, Y. Zhang, M. Carpentieri, A. Fert, G. Finocchio, W. Zhao, and P. Khalili Amiri, Nat. Commun. **12**, 4555 (2021).

[26] V. Krizakova, M. Perumkunnil, S. Couet, P. Gambardella, and K. Garello, J. Magn. Magn. Mater. **562**, 169692 (2022).

[27] H. Kurebayashi, J. H. Garcia, S. Khan, J. Sinova, and S. Roche, Nat. Rev. Phys. **4**, 150 (2022).

[28] F. Sousa, G. Tatara, and A. Ferreira, Phys. Rev. Res. **2**, 043401 (2020).

[29] H. Yang, S. O. Valenzuela, M. Chshiev, S. Couet, B. Dieny, B. Dlubak, A. Fert, K. Garello, M. Jamet, D.-E. Jeong, K. Lee, T. Lee, M.-B. Martin, G. S. Kar, P. Sénéor, H.-J. Shin, and S. Roche, Nature (London) **606**, 663 (2022).

[30] J. Hidding and M. H. D. Guimarães, Front. Mater. **7**, 594771 (2020).

[31] S. Husain, R. Gupta, A. Kumar, P. Kumar, N. Behera, R. Brucas, S. Chaudhary, and P. Svedlindh, Appl. Phys. Rev. **7**, 041312 (2020).

[32] J. Hidding, S. H. Tirion, J. Momand, A. Kaverzin, M. Mostovoy, B. J. van Wees, B. J. Kooi, and M. H. Guimarães, J. Phys. Mater. **4**, 04LT01 (2021).

[33] S. Novakov, B. Jariwala, N. M. Vu, A. Kozhakhmetov, J. A. Robinson, and J. T. Heron, ACS Appl. Mater. Interfaces **13**, 13744 (2021).

[34] Q. Shao, G. Yu, Y.-W. W. Lan, Y. Shi, M.-Y. Y. Li, C. Zheng, X. Zhu, L.-J. J. Li, P. K. Amiri, and K. L. Wang, Nano Lett. **16**, 7514–7520 (2016).

[35] W. Lv, Z. Jia, B. Wang, Y. Lu, X. Luo, B. Zhang, Z. Zeng, and Z. Liu, ACS Appl. Mater. Interfaces **10**, 2843 (2018).

[36] W. Zhang, J. Sklenar, B. Hsu, W. Jiang, M. B. Jungfleisch, J. Xiao, F. Y. Fradin, Y. Liu, J. E. Pearson, J. B. Ketterson, Z. Yang, and A. Hoffmann, APL Mater. **4** (2016).

[37] M. H. D. Guimarães, G. M. Stiehl, D. MacNeill, N. D. Reynolds, and D. C. Ralph, Nano Lett. **18**, 1311 (2018).

[38] I. H. Kao, R. Muzzio, H. Zhang, M. Zhu, J. Gobbo, S. Yuan, D. Weber, R. Rao, J. Li, J. H. Edgar, J. E. Goldberger, J. Yan, D. G. Mandrus, J. Hwang, R. Cheng, J. Katoch, and S. Singh, Nat. Mater. **21**, 1029 (2022).

[39] D. MacNeill, G. M. Stiehl, M. H. D. Guimaraes, R. A. Buhrman, J. Park, and D. C. Ralph, Nat. Phys. **13**, 300 (2017).

[40] D. MacNeill, G. M. Stiehl, M. H. D. Guimarães, N. D. Reynolds, R. A. Buhrman, and D. C. Ralph, Phys. Rev. B **96**, 054450 (2017).

[41] S. Shi, S. Liang, Z. Zhu, K. Cai, S. D. Pollard, Y. Wang, J. Wang, Q. Wang, P. He, J. Yu, G. Eda, G. Liang, and H. Yang, Nat. Nanotechnol. **14**, 945 (2019).

[42] G. M. Stiehl, R. Li, V. Gupta, I. E. Baggari, S. Jiang, H. Xie, L. F. Kourkoutis, K. F. Mak, J. Shan, R. A. Buhrman, and D. C. Ralph, Phys. Rev. B **100**, 184402 (2019).

[43] G. M. Stiehl, D. MacNeill, N. Sivadas, I. El Baggari, M. H. Guimarães, N. D. Reynolds, L. F. Kourkoutis, C. J. Fennie, R. A. Buhrman, and D. C. Ralph, ACS Nano **13**, 2599 (2019).

[44] V. P. Amin, P. M. Haney, and M. D. Stiles, J. Appl. Phys. **128**, 151101 (2020).

[45] A. Veneri, D. T. S. Perkins, and A. Ferreira, Phys. Rev. B **106**, 235419 (2022).

[46] W. Wang, T. Wang, V. P. Amin, Y. Wang, A. Radhakrishnan, A. Davidson, S. R. Allen, T. J. Silva, H. Ohldag, D. Balzar, B. L. Zink, P. M. Haney, J. Q. Xiao, D. G. Cahill, V. O. Lorenz, and X. Fan, Nat. Nanotechnol. **14**, 819 (2019).

[47] T. Seki, Y.-C. Lau, S. Iihama, and K. Takanashi, Phys. Rev. B **104**, 094430 (2021).

[48] M. Aoki, E. Shigematsu, R. Ohshima, T. Shinjo, M. Shiraishi, and Y. Ando, Phys. Rev. B **106**, 174418 (2022).

[49] K. Kang, S. Xie, L. Huang, Y. Han, P. Y. Huang, K. F. Mak, C.-j. Kim, and D. Muller, Nature (London) **520**, 656 (2015).

[50] H. Li, Q. Zhang, C. C. R. Yap, B. K. Tay, T. H. T. Edwin, A. Olivier, and D. Baillargeat, Adv. Funct. Mater. **22**, 1385 (2012).

[51] M. Hayashi, J. Kim, M. Yamanouchi, and H. Ohno, Phys. Rev. B **89**, 144425 (2014).

[52] M. H. Nguyen and C. F. Pai, APL Mater. **9**, 030902 (2021).

[53] N. Roschewsky, E. S. Walker, P. Gowtham, S. Muschinske, F. Hellman, S. R. Bank, and S. Salahuddin, Phys. Rev. B **99**, 195103 (2019).

[54] C. O. Avci, J. Mendil, G. S. Beach, and P. Gambardella, Phys. Rev. Lett. **121**, 087207 (2018).

[55] G. Liu, X. G. Wang, Z. Z. Luan, L. F. Zhou, S. Y. Xia, B. Yang, Y. Z. Tian, G. H. Guo, J. Du, and D. Wu, Phys. Rev. Lett. **127**, 207206 (2021).

[56] K. Zollner, M. D. Petrović, K. Dolui, P. Plecháč, B. K. Nikolić, and J. Fabian, Phys. Rev. Res. **2**, 043057 (2020).

[57] C. F. Schippers, H. J. M. Swagten, and M. H. D. Guimarães, Phys. Rev. Mater. **4**, 084007 (2020).

[58] L. Neumann and M. Meinert, AIP Adv. **8**, 095320 (2018).

[59] R. Yan, J. R. Simpson, S. Bertolazzi, J. Brivio, M. Watson, X. Wu, A. Kis, T. Luo, A. R. Hight Walker, and H. G. Xing, ACS Nano **8**, 986 (2014).